Triple oxygen isotope evidence for limited mid-Proterozoic primary production

Peter W. Crockford[1,2,3*], Justin Hayles[4,5], Huiming Bao[5,6], Noah J. Planavsky[7], Andrey Bekker[8], Philip W. Fralick[9], Galen P. Halverson[1], Thi Hao Bui[1], Yongbo Peng[5], and Boswell A. Wing[10]

[1]McGill University 3450 University Street Montreal, QC H3A0E8, Canada
[2]Weizmann Institute of Science, Rehovot 76100, Israel
[3]Princeton University, Princeton New Jersey 08544, USA
[4]Rice University 6100 Main St. Houston, TX 77005, USA
[5]Louisiana State University Howe Russel Building, Baton Rouge, LA 70803, USA
[6] School of Earth & Space Sciences, Peking University, Beijing 100871, China
[7]Yale University 210 Whitney Ave., New Haven CT 06511, USA
[8]University of California Riverside, 900 University Ave. Riverside CA 92521, USA
[9]Lakehead University. 955 Oliver Rd. Thunder Bay Ontario, P7B 5E1, Canada
[10]University of Colorado Boulder, UCB 399, Boulder, Colorado 80309, USA

*Corresponding Author E-mail: peter.crockford@mail.mcgill.ca

Abstract: Before the rise of complex eukaryotic ecosystems the global biosphere is commonly assumed to have been less productive than today[1]. However, direct evidence for this assertion is lacking. Here we present triple oxygen isotope measurements ($\Delta^{17}O$) from ca. 1.4 Ga sedimentary sulfates from the Sibley Basin of Ontario Canada that provide evidence for a less productive biosphere in the mid-Proterozoic. We report the most negative $\Delta^{17}O$ values (down to -0.88‰) observed in sulfate except for those from the terminal Cryogenian period[2]. This observation demonstrates that the mid-Proterozoic (≈1.8-0.8 Ga) atmosphere was dissimilar to more recent ones, directly reflecting a unique interplay among the atmospheric partial pressures of CO_2 and O_2 (pCO_2, pO_2) and the photosynthetic O_2 flux at this time[3]. As oxygenic gross primary production (*GPP*) is stoichiometrically related to photosynthetic O_2 flux, under current estimates of Proterozoic pCO_2 (2-30 times Pre-Anthropogenic Levels [PAL]), our modeling indicates that mid-Proterozoic *GPP* was ≈6% PAL if Proterozoic pO_2 was between 0.1-1% PAL and ≈41% PAL if pO_2 were higher (1-10% PAL). When compared to estimates of Archean[4-6] and Phanerozoic primary production[7], these solutions show that an increasingly more productive biosphere accompanied the broad secular pattern of increasing atmospheric O_2 over geologic time[8].

Modern primary producers perform oxygenic photosynthesis, providing O_2 to the atmosphere and fixing carbon that fuels heterotrophic consumption in the global biosphere. In the low-O_2 mid-Proterozoic world[8], this oxygenic gross primary production (*GPP*) has been widely assumed to be less than *GPP* in more recent times[1]. Accordingly, mechanistic explanations for low-O_2 Proterozoic surface environments focus on how to limit the productivity of the Proterozoic biosphere[9-11], despite the lack of direct empirical evidence for lower Proterozoic *GPP*. Indeed, proposals for sustaining Proterozoic environmental stasis[12-14] would be strengthened, if their key component could be validated from the geologic record. Here we examine whether the mid-Proterozoic biosphere was less productive than more recent ones utilizing a triple oxygen isotope proxy for *GPP* in ca. 1.4 Ga sulfate minerals.

A record of the productivity of the biosphere is embedded within the mass-independent oxygen isotope fractionation (O-MIF) carried by tropospheric O_2. Stratospheric photochemical reactions preferentially concentrate ^{17}O and ^{18}O in O_3, leaving ^{16}O anomalously enriched in the residual O_2, which, therefore, has a negative $\Delta^{17}O$ value ($\Delta^{17}O = \delta^{17}O - 0.5305 \times \delta^{18}O$). Isotopic exchange between stratospheric CO_2 and heavy oxygen atoms from O_3 photolysis imparts a positive $\Delta^{17}O$ value to CO_2[15]. Mass balance dictates that O_2 exiting the stratosphere carries a negative $\Delta^{17}O$ value and that the magnitude of this anomaly is proportional to pCO_2 levels[16]. In the troposphere, stratospheric O_2 mixes with O_2 produced through photosynthesis that carries ^{16}O, ^{17}O, and ^{18}O in isotopically normal proportions, with a near-zero $\Delta^{17}O$ value set by the isotopic composition of water[17]. The $\Delta^{17}O$ value of tropospheric O_2 reflects the relative contributions of O_2 supplied from the stratosphere versus O_2 derived from photosynthesis[17,18].

This balance is only interpretable if there is enough atmospheric O_2 to sustain a sizable ozone layer (pO_2 >0.1% Pre-Anthropogenic Level [PAL]; 100% PAL = 209500 ppm O_2)[19]. Although stratospheric oxygen dynamics do not permit the production of O-MIF below this pO_2, such atmospheric anoxia supports the photochemical production of sulfur-isotope mass-independent fractionation (S-MIF). As seen in the Archean rock record, the presence of S-MIF and absence of O-MIF provides a key metric to identify a strictly anoxic atmosphere[20] (Extended Data Table 1). At higher pO_2, since photosynthetic carbon fixation is proportional to O_2 production through the photosynthetic quotient, the $\Delta^{17}O$ anomaly in tropospheric O_2 is a direct measure of *GPP*[17]. With independent estimates of contemporaneous pCO_2 and sufficient pO_2, the $\Delta^{17}O$ value of ancient atmospheric O_2 can constrain ancient *GPP*[7].

Sedimentary sulfate minerals can preserve a record of ancient atmospheric O_2. Oxidative weathering of sulfide minerals incorporates a sizeable fraction of oxygen from tropospheric O_2 into product sulfate (denoted f_{O_2}). Biologically mediated pyrite oxidation, which dominates abiotic oxidation in natural environments[21], produces a range of f_{O_2} between 8-15%[22]. The $\Delta^{17}O$ value of aqueous sulfate is also influenced by the ratio of sulfide to sulfate minerals in the source rocks undergoing oxidative weathering as well as the intensity and style of microbial sulfur cycling in the aqueous environment[23,24], which erases the $\Delta^{17}O$ signal. Modern marine sulfate, for example, carries a muted but resolvable negative average $\Delta^{17}O$ value[2] ($\Delta^{17}O \approx -0.08‰$; Extended Data Table 1) inherited from modern tropospheric O_2 (≈ -0.55‰[25]). Terrestrial sulfate-rich evaporative settings are more conducive than marine settings to rapid precipitation of gypsum, anhydrite, or other sulfate salts[26], thereby minimizing the isotopic consequences of microbial recycling[27] and capturing newly formed sulfate with a $\Delta^{17}O$ value that more directly reflects tropospheric O_2.

The Rossport Formation of the Sibley Group in Ontario, Canada contains lacustrine and sabkha sediments with abundant gypsum layers and nodules. These sulfate-rich sediments are intruded by 1.1 Ga dykes, and have an estimated depositional age of ca. 1.4 Ga[28] (Supplementary Information). We measured the oxygen ($\delta^{18}O$, $\Delta^{17}O$) and sulfur ($\delta^{34}S$, $\Delta^{33}S$) isotope compositions of sulfate chemically extracted from 68 Sibley samples. We found $\Delta^{17}O$ values more negative than those of modern and Phanerozoic marine sulfates as well as that of modern tropospheric O_2 (Fig. 1), and no evidence of S-MIF (Extended Data Table 1). Our results unambiguously provide the first near-direct record of mid-Proterozoic atmospheric O_2 and indicate that the bulk atmosphere has existed in three isotopically distinct states over Earth's history: S-MIF but no O-MIF (Archean), O-MIF but no S-MIF (Proterozoic), and no significant O-MIF or S-MIF (Phanerozoic)[2,20] (Extended Data Table 1).

Unlike syn-glacial Cryogenian sulfate (Extended Data Fig. 1), the low $\delta^{34}S$, small negative $\Delta^{33}S$, and high $\delta^{18}O$ values reported here suggest weak microbial sulfur cycling and limited sulfide re-oxidation[29,30] in the Sibley basin (Fig. 2). The $\Delta^{17}O$ values of the Sibley Group sulfates, therefore, are primarily modulated by the amount of O_2 incorporated during sulfide oxidation rather than weathering and re-deposition of pre-existing sulfate minerals or intense re-oxidative microbial sulfur cycling (Fig. 2). Considering likely f_{O_2} values of pyrite oxidation (8-15%[22]), the most negative Sibley $\Delta^{17}O$ value (-0.88‰, Extended Data Table 1) implies that coeval tropospheric O_2 had a $\Delta^{17}O$ value between -11 to -6‰. This range is ≈10 to 20 times larger than the $\Delta^{17}O$ of modern tropospheric O_2, demonstrating that the mid-Proterozoic atmosphere bore little resemblance to the modern with respect to the magnitude of its stratospheric and photosynthetic O_2 fluxes as well as the size of the O_2 reservoir where these fluxes competed.

Although mid-Proterozoic $\Delta^{17}O$ and *GPP* cannot be calibrated from modern values[2,25], isotope mass balance calculations indicate that the $\Delta^{17}O$ value of tropospheric O_2 reflects three key variables: pCO_2, pO_2, and *GPP* with parameters like troposphere-stratosphere exchange exerting considerably less influence[3]. Under near-modern *GPP*, as may have characterized the immediate aftermath of the terminal Cryogenian glaciation[31], ultra-high atmospheric pCO_2 (>350 times PAL; 1 PAL = 280 ppm CO_2) is the only viable way to impart a significantly negative $\Delta^{17}O$ value to tropospheric O_2[2,3]. In lower pCO_2 conditions, however, similarly negative $\Delta^{17}O$ values can be generated if *GPP* is greatly diminished, which effectively lengthens the residence time of photosynthetic O_2 in the atmosphere[3]. We used this isotope mass balance approach[3] together with independent estimates for mid-Proterozoic pCO_2 and pO_2 levels to show that Sibley sulfate $\Delta^{17}O$ values provide the first empirical evidence that limited mid-Proterozoic primary production was a biogeochemical reality.

Estimates of mid-Proterozoic pCO_2 from geochemical proxies and climate models suggest pCO_2 between 2-30 PAL at 1.4 Ga (Extended Data Fig. 2). Mid-Proterozoic O_2 estimates span a wider relative range but fall between 0.1-10% PAL (Extended Data Fig. 2). We take an agnostic perspective of the techniques for estimating pO_2 and pCO_2 and use uniform frequency distributions within these ranges as the basis for a Monte Carlo resampling of mid-Proterozoic O_2 and CO_2 levels. Along with a resampling of other control parameters in the isotope mass-balance model (Extended Data Fig. 3), this enabled us to turn our measured $\Delta^{17}O$ distribution (Fig. 1) into bootstrap estimates for mid-Proterozoic *GPP* (Methods). The Monte Carlo estimates confirm that it is very likely that the mid-Proterozoic biosphere was less productive than the present biosphere, with >93% of the *GPP* estimates less than pre-anthropogenic levels (Fig. 3).

There is a small tail of relative *GPP* values above 100% PAL that require sulfate $\Delta^{17}O$ approaching zero, f_{O_2} near the maximum likely value, and, importantly, pO_2 close to 10% PAL (Extended Data Fig. 4). These extreme circumstances, though permitted by our analysis, were unlikely to have been persistent on the mid-Proterozoic Earth if present at all. Mid-Proterozoic *GPP* estimates are always strongly influenced by pO_2 (Extended Data Fig. 4B), which suggests that the bimodal structure of the *GPP* probability density (Fig. 3) is a consequence of the wide range of pO_2 values that we used in the Monte Carlo calculations. Under more restricted ranges of pO_2, the bimodality disappears and the estimated probability densities for *GPP* take on a normal form (Extended Data Fig. 5; Methods). To explore this behavior, we fit the full suite of

GPP results to a pair of gaussian probability density functions, one with a mean *GPP* of 6±1% PAL that is representative of low O_2 conditions (0.1 to 1% PAL) and another with a mean *GPP* of 41±3% PAL (quoted uncertainties are 95% confidence intervals on the mean; Fig. 3) that is representative of high O_2 conditions (1 to 10% PAL). The lower *GPP* state is consistent with lower mean pO_2 (≈0.3% PAL) while the higher *GPP* state corresponds to higher mean pO_2 (≈2% PAL; Extended Data Fig. 5). The trajectory of these estimates reflects the positive co-variation between *GPP* and pO_2 that scales across a range of *GPP*-pO_2 values (Extended Data Fig. 4B).

Approximately 700-800 million years after the deposition of the Sibley sulfates, there was a major ecological shift in the marine realm, with a cyanobacterial phytoplankton population replaced by one dominated by algae[32]. The ecological transition has been linked to a rise in nutrient levels[12], consistent with eukaryotic predominance in more nutrient-rich regions of the modern oceans[33]. In light of the timing of this transition and the marked similarity of our higher *GPP* estimate to algal-dominated primary production in today's ocean (≈45% of the primary production of the modern biosphere[34]), we suggest that our lower *GPP* estimate (and, as a result, a lower pO_2) is more likely to reflect the mid-Proterozoic world. Enhanced regenerated production in a bacteria-dominated, oligotrophic marine ecosystem[35,36] could have supported higher overall *GPP* in nutrient-limited Proterozoic oceans[1]. However, there is evidence that intense heterotrophic recycling of carbon only appeared in planktonic ecosystems in the latest Proterozoic[32,37,38] providing further support for our lower *GPP*-pO_2 estimates. While reduced Proterozoic *GPP* is typically linked to the need to throttle O_2 generation on geologic timescales via diminished export production and organic carbon burial[9,11,12], the *GPP*-pO_2 co-variation described here highlights that diminished O_2 production may have also directly led to reduced O_2 levels on the Proterozoic Earth. Along with Archean[4-6] and Phanerozoic[7] *GPP* estimates that bookend our inferred Proterozoic *GPP* (≈6% PAL), this relationship implies that primary production has progressively increased in concert with the broad two-step history of O_2 in Earth's atmosphere[8].

References:

1. Anbar, A. D., Knoll, A. H. Proterozoic ocean chemistry and evolution: a bioinorganic bridge? *Science*. **297**. 1137-1142 (2002).

2. Bao, H., Lyons, J. R., Zhou, C. Triple oxygen isotope evidence for elevated CO_2 levels after a Neoproterozoic glaciation. *Nature*. **453**, 504-506 (2008).

3. Cao, X., Bao, H. Dynamic model constraints on oxygen-17 depletion in atmospheric O_2 after a snowball Earth. *Proc. Natl. Acad. Sci. USA.* **110**, 14546-14550 (2013).

4. Kharecha, P., Kasting, J., Siefert, J. A coupled atmosphere–ecosystem model of the early Archean Earth. *Geobiology*. **3**, 53-76 (2005).

5. Canfield, D. E., Rosing, M. T., Bjerrum, C. Early anaerobic metabolisms. *Philos. Trans. R. Soc. London Ser. B*. **361**, 1819-1836 (2006).

6. Ward, L. M., Kirschvink, J. L., Fischer, W. W. Timescales of Oxygenation Following the Evolution of Oxygenic Photosynthesis. *Orig. Life Evol. Biosph*. **46**, 51-65 (2016).

7. Wing, B. A. A cold, hard look at ancient oxygen. *Proc. Natl. Acad. Sci. USA.* **110**, 14514-14515 (2013).

8. Lyons, T. W., Reinhard, C. T., Planavsky, N. J. The rise of oxygen in Earth's early ocean and atmosphere. *Nature*. **506**, 307-315 (2014).

9. Laakso, T. A., Schrag, D. P. Regulation of atmospheric oxygen during the Proterozoic. *Earth Planet. Sci. Lett*. **388**, 81-91 (2014).

10. Sánchez-Baracaldo, P., Ridgwell, A., Raven, J. A. A Neoproterozoic transition in the marine nitrogen cycle. *Curr. Biol*. **24**, 652-657 (2014).

11. L. A. Derry, Causes and Consequences of mid-Proterozoic Anoxia. *Geophys. Res. Lett.* **42***,* 8538-8546 (2015).

12. Reinhard, C. T. *et al.* Evolution of the global phosphorus cycle. *Nature.* **541**, 386-389 (2016*)*.

13. Koehler, M.C. *et al.* Spatial and temporal trends in Precambrian nitrogen cycling: a Mesoproterozoic offshore nitrate minimum. *Geochim. Cosmochim. Acta*. **198**, 315-337 (2017).

14. Buick, R., Des Marais, D.J. and Knoll, A.H. Stable isotopic compositions of carbonates from the Mesoproterozoic Bangemall Group, northwestern Australia. *Chem. Geol.* **123**, 153-171 (1995).

15. Wen, J., Thiemens, M. H. Multi-isotope study of the O (1 D)+ CO_2 exchange and stratospheric consequences. *J. Geophys. Res*. **98**, 12801-12808 (1993).

16. Yung, Y. L., DeMore, W. B., Pinto, J. P. Isotopic exchange between carbon dioxide and ozone via O (1D) in the stratosphere. *Geophys. Res. Lett*. **18,** 13-16 (1991).

17. Luz, B., Barkan, E., Bender, M. L., Thiemens, M. H., Boering, K. A. Triple-isotope composition of atmospheric oxygen as a tracer of biosphere productivity. *Nature*. **400**, 547-550 (1999).

18. Bender, M. L., Sowers, T., Labeyrie, L. The Dole effect and its variations during the last 130,00 years as measured in the Vostok ice core. *Global Biogeochem. Cycles*. **8**, 363-376 (1994).

19. Segura, et al. Ozone concentrations and ultraviolet fluxes on Earth-like planets around other stars. *Astrobiol.* **3**, 689-708 (2003).

20. Bao, H., Rumble, D., Lowe, D.R., The five stable isotope compositions of Fig Tree barites: Implications on sulfur cycle in ca. 3.2 Ga oceans. *Geochim, Cosmochim. Acta*. **71**, 4868-4879 (2007).

21. Percak-Dennett, E. *et al.* 2017. Microbial acceleration of aerobic pyrite oxidation at circumneutral pH. *Geobiology* (*in press*).

22. Balci, N., Shanks III, W. C., Mayer, B., Mandernack, K. W. Oxygen and sulfur isotope systematics of sulfate produced by bacterial and abiotic oxidation of pyrite. *Geochim. Cosmochim. Acta*. **71***,* 3796-3811 (2007).

23. Antler, G., Turchyn, A. V., Rennie, V., Herut, B., Sivan, O. Coupled sulfur and oxygen isotope insight into bacterial sulfate reduction in the natural environment. *Geochim. Cosmochim. Acta*. **118**, 98-117 (2013).

24. Pellerin, A. *et al.* Mass-dependent sulfur isotope fractionation during reoxidative sulfur cycling: A case study from Mangrove Lake, Bermuda. *Geochim. Cosmochim. Acta*. **149**, 152-164 (2015).

25. Pack, A. *et al.* Tracing the oxygen isotope composition of the upper Earth's atmosphere using cosmic spherules. *Nat. Comm.*, **8**, (2017).

26. Hardie, L. A. The origin of the recent non-marine evaporite deposit of Saline Valley, Inyo County, California. *Geochim. Cosmochim. Acta*. **32**, 1279-1301 (1968).

27. Ryu, J. H., Zierenberg, R. A., Dahlgren, R. A., Gao, S. Sulfur biogeochemistry and isotopic fractionation in shallow groundwater and sediments of Owens Dry Lake, California. *Chem. Geol*. **229***,* 257-272 (2006).

28. Rogala, B., Fralick, P. W., Heaman, L. M., Metsaranta, R. Lithostratigraphy and chemostratigraphy of the Mesoproterozoic Sibley Group, northwestern Ontario, Canada. *Can. J. Earth Sci*. **44**, 1131-1149 (2007).

29. Bao, H., Fairchild, I. J., Wynn, P. M., Spötl, C. Stretching the envelope of past surface environments: Neoproterozoic glacial lakes from Svalbard. *Science*. **323**, 119-122 (2009).

30. Johnston, D.T. *et al.* Active microbial sulfur disproportionation in the Mesoproterozoic. *Science*, **310** 1477-1479 (2005).

31. Kunzmann, M., *et al.* Zn isotope evidence for immediate resumption of primary productivity after snowball Earth. *Geology*. **41**, 27-30 (2013).

32. Brocks J. J., *et al.* The rise of algae in Cryogenian oceans and the emergence of animals. *Nature*. **548**, 578-581 (2017)

33. Ward, B.A., Dutkiewicz, S. and Follows, M.J. Modelling spatial and temporal patterns in size-structured marine plankton communities: top–down and bottom–up controls. *J. Plank. Res.* **36(1)**, 31-47. (2013)

34. Field, C.B., Behrenfeld, M.J., Randerson, J.T. and Falkowski, P., Primary production of the biosphere: integrating terrestrial and oceanic components. *Science*, **281**, 237-240 (1998)

35. Eppley, R.W. and Peterson, B.J. Particulate organic matter flux and planktonic new production in the deep ocean. *Nature*, **282**, 677-680 (1979)

36. Close, H.G., *et al.* Export of submicron particulate organic matter to mesopelagic depth in an oligotrophic gyre. *Proc. Natl. Acad. Sci. USA* **110**, 12565-12570 (2013)

37. Logan, G.A., Hayes, J.M., Hieshima, G.B. and Summons, R.E. Terminal Proterozoic reorganization of biogeochemical cycles. *Nature*, **376**, 53-56 (1995)

38. Close, H.G., Bovee, R. and Pearson, A., Inverse carbon isotope patterns of lipids and kerogen record heterogeneous primary biomass. *Geobiology*, **9**, 250-265 (2011).

39. Peng, Y., Bao, H., Zhou, C., Yuan, X. ^{17}O-depleted barite from two Marinoan cap dolostone sections, South China. *Earth Planet. Sci. Lett.* **305**, 21-31 (2011).

40. Killingsworth, B. A., Hayles, J. A., Zhou, C., Bao, H. Sedimentary constraints on the duration of the Marinoan Oxygen-17 Depletion (MOSD) event. *Proc. Natl. Acad. Sci. USA.* **110**, 17686-17690 (2013).

41. Crockford, P.W., et al. Linking Paleocontinents through triple oxygen isotope anomalies. *Geology*. **46(2)**, 179-182 (2018)

42. H. Bao, Z. Q. Chen, C. Zhou, An ^{17}O record of late Neoproterozoic glaciation in the Kimberley region, Western Australia. *Precambrian Res*. ***216***, 152-161 (2012).

43. Crockford, P. W. *et al.* Triple oxygen and multiple sulfur isotope constraints on the evolution of the post-Marinoan sulfur cycle. *Earth Planet. Sci. Lett*. **435**, 74-83 (2016).

44. Cowie, B. R., Johnston, D. T. High-precision measurement and standard calibration of triple oxygen isotopic compositions (δ^{18}O, Δ'^{17}O) of sulfate by F_2 laser fluorination. *Chem. Geol.* **440**, 50-59 (2016).

45. Sim, M.S., Bosak, T. and Ono, S. Large sulfur isotope fractionation does not require disproportionation. *Science*, **333,** 74-77 (2011)

46. Davis, D. W., Sutcliffe, R. H. U-Pb ages from the Nipigon plate and northern Lake Superior. *Geol. Soc. Am. Bull.* **96**, 1572-1579 (1985).

47. Franklin, J. M. The Sibley Group, Ontario. *Rubidium–strontium isotopic age studies, report*. **2**, 77-14 (1978).

48. Robertson, W. A. Pole position from thermally cleaned Sibley Group sediments and its relevance to Proterozoic magnetic stratigraphy. *Can. J. Earth Sci.* **10**, 180-193 (1973).

49. Elston, D. P., Enkin, R. J., Baker, J. D., Kisilevsky, K. Tightening the Belt: paleomagnetism-stratigraphic constraints on deposition, correlation, and deformation of the Middle Proterozoic (ca. 1.4 Ga) Belt-Purcell Supergroup, United States and Canada. *Geol. Soc. Am. Bull.* **114**, 619-638 (2002).

50. Cheadle, B. A. Alluvial-playa sedimentation in the lower Keweenawan Sibley Group, Thunder Bay District, Ontario. *Can. J. Earth Sci.* **23**, 527-542 (1986).

51. R. T. Metsaranta, thesis, Lakehead University (2006).

52. Bao, H. Purifying barite for oxygen isotope measurement by dissolution and reprecipitation in a chelating solution. *Anal. Chem.* **78**, 304-309 (2006).

53. Bao, H. Thiemens, M.H. Generation of O_2 from $BaSO_4$ using a CO_2- laser fluorination system for simultaneous analysis of $\delta^{18}O$ and $\delta^{17}O$. *Anal. Chem.* **72**, 4029-4032 (2000).

54. Matsuhisa, Y. Goldsmith, J. R., Clayton, R. N. Mechanisms of hydrothermal crystallization of quartz at 250°C and 15 kbar. *Geochim. Cosmochim. Acta*. **42**, 173-182 (1978).

55. Cao, X., Liu, Y. Equilibrium mass-dependent fractionation relationships for triple oxygen isotopes. *Geochim. Cosmochim. Acta*. **75**, 7435-7445 (2011).

56. Bao, H., Cao, X., Hayles, J. A. Triple Oxygen Isotopes: Fundamental Relationships and Applications. *Annu. Rev. Earth Planet. Sci*. **44**, 463-492 (2016).

57. Miller, M. F. Isotopic fractionation and the quantification of ^{17}O anomalies in the oxygen three-isotope system: an appraisal and geochemical significance. *Geochim. Cosmochim. Acta*. **66**, 1881-1889 (2002).

58. Angert, A., Rachmilevitch, S., Barkan, E., Luz, B. Effects of photorespiration, the cytochrome pathway, and the alternative pathway on the triple isotopic composition of atmospheric O_2. *Global Biogeochem. Cycles*. **17,** 1030 (2003).

59. Thode, H. G., Monster, J., Dunford, H. B. Sulphur isotope geochemistry. *Geochim. Cosmochim. Acta*. **25**, 159-174 (1961).

60. Shaheen, R., Janssen, C., Röckmann, T. Investigations of the photochemical isotope equilibrium between O_2, CO_2 and O_3. *Atmos. Chem. Phys*. **7**, 495-509 (2007).

61. von Paris, P., *et al.* Warming the early Earth CO_2 reconsidered. *Planet. Space Sci*. **56**, 1244-1259 (2008).

62. Wolf, E. T. Toon, O. B. Controls on the Archean Climate System Investigated with a Global Climate Model. *Astrobiology*. **14**, 241-253 (2014).

63. Mills, B., Lenton, T. M., Watson, A. J. Proterozoic oxygen rise linked to shifting balance between seafloor and terrestrial weathering. *Proc. Natl. Acad. Sci. USA.* **111**, 9073-9078 (2014).

64. Kaufman, A. J., Xiao, S. High CO_2 levels in the Proterozoic atmosphere estimated from analyses of individual microfossils. *Nature*. **425**, 279-282 (2003).

65. Sheldon, N. D. Causes and consequences of low atmospheric $p\mathrm{CO}_2$ in the Late Mesoproterozoic. *Chem. Geol*. **362**, 224-231 (2013).

66. Hansen, J., *et al.* Target atmospheric CO_2: Where should humanity aim? *arXiv preprint arXiv:0804.1126* (2008).

67. Kasting, J. F., Donahue, T.M. The evolution of atmospheric ozone. *J. Geophys. Res.: Oceans*, **85**, 3255-3263 (1980).

68. Pavlov AA, and Kasting JF. Mass-independent fractionation of sulfur isotopes in Archean sediments: strong evidence for an anoxic Archean atmosphere. *Astrobiology*. **2**, 27-41 (2002)

69. Horner, T.J., et al. Pelagic Barite Precipitation at micromolar ambient sulphate. *Nat. Comm.* **8**, 1342. (2017)

70. Holland, H. D., Feakes, C. R., Zbinden, E. A. The Flin Flon paleosol and the composition of the atmosphere 1.8 BYBP. *Am. J. Sci*. **289**, 362-389 (1989).

71. Planavsky, N. J., *et al.* Low Mid-Proterozoic atmospheric oxygen levels and the delayed rise of animals. *Science*. **346**, 635-638 (2014).

72. Cole, D. B., *et al.* A shale-hosted Cr isotope record of low atmospheric oxygen during the Proterozoic. *Geology*. **44***, 555-558* (2016).

73. Gilleaudeau, G.J. *et al.* Oxygenation of the mid-Proterozoic atmosphere: clues from chromium isotopes in carbonates. *Geochem.l Per. Lett.*, **2**, 178-187 (2016).

74. Zhang, S., *et al.* Sufficient oxygen for animal respiration 1,400 million years ago. *Proc. Natl. Acad. Sci. USA.* **113**, 1731-1736 (2016).

75. Planavsky N. J. *et al*. No evidence for high atmospheric oxygen levels 1,400 million years ago. *Proc. Natl. Acad. Sci. USA*. **113**, E2550-E2551 (2016).

76. Liu, X. M. *et al.* Tracing Earth's O_2 evolution using Zn/Fe ratios in marine carbonates. *Geochem. Perspect. Lett*. **2**, 24-34 (2016).

77. Canfield, D.E. A new model for Proterozoic ocean chemistry. *Nature*, **396**, 450-453, (1998).

78. Reinhard, C.T., et al. Proterozoic ocean redox and biogeochemical stasis. *Proc. Natl. Acad. Sci.* **110**, 5357-5362 (2013.

79. Cox, G.M., *et al*. Basin redox and primary productivity within the Mesoproterozoic Roper Seaway. *Chem. Geol.* **440**, 101-114 (2016).

80. Daines, S. J., Mills, B., Lenton, T. M. Atmospheric oxygen regulation at low Proterozoic levels by incomplete oxidative weathering of sedimentary organic carbon. *Nature Commun.* 10.1038/ncomms14379 (2017).

81. Runnegar, B. Precambrian oxygen levels estimated from the biochemistry and physiology of early eukaryotes. *Global Planet. Change*. **5**, 97-111 (1991).

82. Sperling, E. A., Halverson, G. P., Knoll, A. H., Macdonald, F. A., Johnston, D. T. A basin redox transect at the dawn of animal life. *Earth Planet. Sci. Lett*. **371**, 143-155 (2013).

83. Mills, D. B. *et al.* Oxygen requirements of the earliest animals. *Proc. Natl. Acad. Sci. USA.* **111**, 4168-4172 (2014).

84. Kohl, I., Bao, H. Triple-oxygen-isotope determination of molecular oxygen incorporation in sulfate produced during abiotic pyrite oxidation (pH= 2–11). *Geochim. Cosmochim. Acta*. **75**, 1785-1798. (2011).

85. Bao, H., Cao, X. and Hayles, J.A. Triple oxygen isotopes: fundamental relationships and applications. *Ann. Rev. Earth Planet. Sci.* **44**, 463-492. (2016).

86. Hayles, J.A., Cao, X. and Bao, H. The statistical mechanical basis of the triple isotope fractionation relationship. *Geochem. Per. Lett.* **3**, 1-11. (2017).

87. Trenberth, K., Smith, E. L. The mass of the atmosphere: A constraint on global analyses. *J. Clim*. **18**, 864-875 (2005).

88. Linz, M. *et al.* The strength of the meridional overturning circulation of the stratosphere. *Nature Geoscience* (2017).

89. Butchart, N. *et al.* Simulations of anthropogenic change in the strength of the Brewer–Dobson circulation. *Clim. Dynamics* **27,** 727-741 (2006).

90. Fiorella, R.P. and Sheldon, N.D. Equable end Mesoproterozoic climate in the absence of high CO_2. *Geology*, **45**, 231-234 (2017).

91. Gibson, T.M., et al. Precise age of Bangiomorpha pubescens dates the origin of eukaryotic photosynthesis. *Geology*. **46(2)**, 135-138 (2018)

92. Kah, L.C. and Riding, R. Mesoproterozoic carbon dioxide levels inferred from calcified cyanobacteria. *Geology*, **35**, 799-802 (2017).

93. Farquhar, J., Bao, H. and Thiemens, M. Atmospheric influence of Earth's earliest sulfur cycle. *Science*, **289**, 756-758 (2000).

94. Goldblatt, C., Lenton, T.M. and Watson, A.J. Bistability of atmospheric oxygen and the Great Oxidation. *Nature*, **443**, 683-686 (2006).

Figure Captions:

Figure 1. Triple oxygen isotope data over the past 1.5 billion years. Compiled $\Delta^{17}O$ data in barites (white diamonds)[2,39-41,43], carbonate-associated sulfate (CAS; grey triangles)[29,42], and evaporites (grey or red circles)[2]. Analytical uncertainty on $\Delta^{17}O$ measurements (1σ) is less than 0.05‰. Results are compared to average $\Delta^{17}O$ values of modern marine sulfate[2,44] (dark blue dashed line) and modern tropospheric O_2[25] (light blue dashed line). Inset is a histogram of $\Delta^{17}O$ values from the samples analyzed here.

Figure 2. Sulfur and oxygen isotope constraints on limited microbial sulfur cycling in Sibley basin. (A) $\delta^{34}S$ and $\Delta^{17}O$ values exhibit a weak positive correlation (n = 64; $R^2 = 0.132$ (Pearson's)), showing that microbial sulfur cycling was not effective in removing anomalous $\Delta^{17}O$ values; (B) $\delta^{34}S$ and $\Delta^{33}S$ values indicate a sulfur cycle dominated by dissimilatory sulfate reduction, (DSR; grey field)[30,45] with no evidence for a re-oxidative flux into the sulfate pool ($f_{r\text{-}o}$: fraction of sulfide that is reoxidized to sulfate); (C) steeply aligned $\delta^{34}S$ and $\delta^{18}O$ values imply relatively slow sulfate reduction rates (SRR)[23]. Total analytical uncertainty on $\delta^{34}S$, $\Delta^{33}S$ and $\delta^{18}O$ measurements is estimated at 0.1, 0.01 and 0.5‰ respectively.

Figure 3. Empirical probability densities of Mid-Proterozoic Gross Primary Production. Monte Carlo solutions are based on the measured distribution of $\Delta^{17}O$ values of the ≈1.4 Ga Sibley sulfates, and take into account uncertainties in the control parameters of the isotope-mass-balance model. The grey histogram represents the full suite of estimates and is well approximated as the sum of a pair of gaussian probability density functions (root-mean-squared error = 0.001; Methods). The red line represents the probability density function for *GPP* solutions when pO_2 levels are between 1-10% PAL and is characterized by a mean *GPP* value of 41±3% PAL (uncertainties are 95% confidence intervals on the mean). The yellow line represents the probability density function for *GPP* solutions when pO_2 levels are between 0.1-1% PAL and is characterized by a mean *GPP* value of 6±1% PAL.

Figure 1:

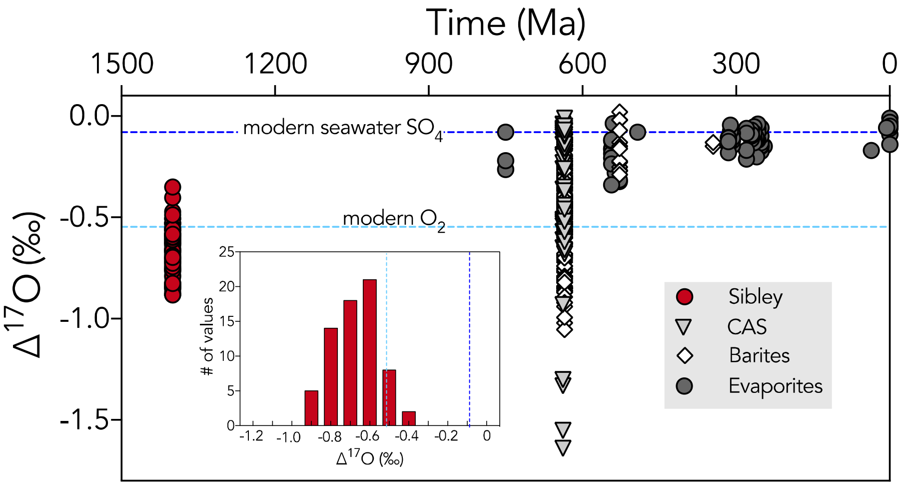

Figure 2:

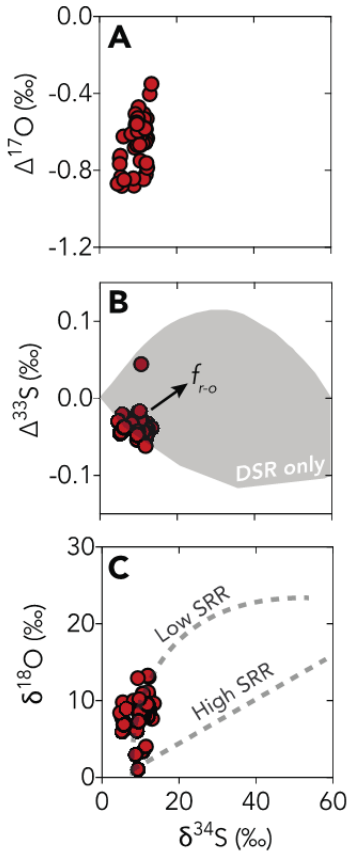

Figure 3:

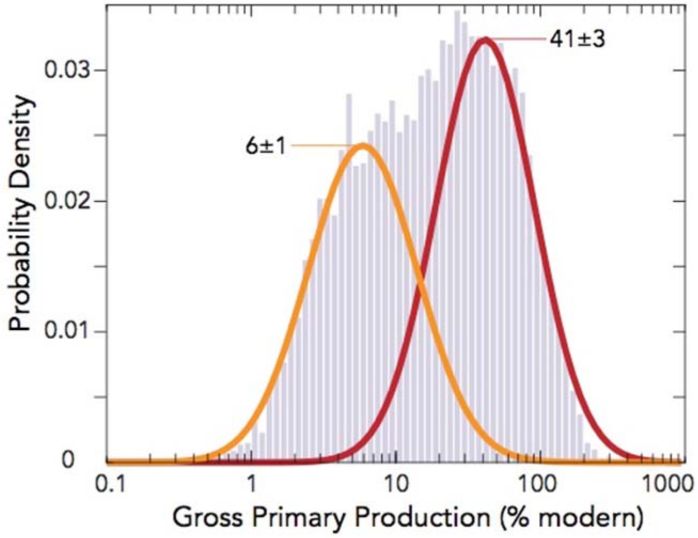

Acknowledgements PWC acknowledges funding from a Natural Sciences and Engineering Research Council of Canada (NSERC) PGS-D grant. This research was supported by funding from NSERC, the Fonds de Recherche du Québec–Nature et Technologies, and the University of Colorado Boulder (BAW). HB acknowledges funding from the strategic priority research program (B) of CAS (XDB18010104. We thank Eric Wolf, Nick Cowan, Stephen Becker, Yolanda Slichter, and Lou Derry for discussions on the assumptions, methods and implications of our study.

Author Contributions PWC and BAW designed research. NJP, AB, and PF provided samples. PWC, JAH, YP and THB performed isotopic analyses. PWC and BAW conducted modeling. PWC wrote the manuscript with contributions from BAW, NJP and AB, and input from all co-authors.

Competing Interests

The authors declare no competing financial interests.

Author information Correspondence and requests for materials should be addressed to PWC (peter.crockford@weizmann.ac.il).

Methods:

Sample Information

Sample Locations: Sediments of the Sibley Group were deposited over an approximately 70,000 km^2 area that extends into northern Lake Superior, and to the margins of Lake Nipigon in Ontario, Canada (Extended Data Fig. 6). While the surface expression of the Sibley Group is typically poor, extensive mineral exploration in the area has provided kilometers of drill core. For this study, 68 samples were collected from four different drill cores: NI-92-7 (UTM east 353850, north 5443000), NB-97-2 (UTM east 426990 north 5416241), NB-97-4 (UTM east 425430 north 5410540) and WP-07-03 (UTM east 379602 north 5422047).

Age Constraints: Maximum age constraints for the entire Sibley Group are provided by rhyolites that unconformably underlie the Sibley Group with a U-Pb age of 1530.5 +/- 6.2 Ma[46]. A minimum age is constrained by cross-cutting diabase sills dated at 1109.7 +/- 2 Ma[46]. The only age measured directly on Sibley Group material is provided by a whole-rock Rb-Sr isochron that gave a calculated minimum age of 1339 +/- 33 Ma for the Kama Hill Formation shales[47]. Paleomagnetic pole positions place the Sibley Group[48] on the apparent polar wander path of the Belt Supergroup at ca. 1.4 Ga[49]. In light of these constraints and the stratigraphic location of the Rossport Formation below the Kama Hill Formation (see below) we consider the approximate age of the material analyzed for this study to be ca. 1.4 Ga.

Depositional Setting: Gypsum nodules used in this study were taken from the Firehill member of the Rossport Formation, which was deposited after the fluvial to near shore lacustrine sandstones and conglomerates of the Pass Lake Formation and before the saline mud-flats of the Kama Hill Formation (Ref. 28 main text). The Rossport Formation is subdivided into three members beginning with the Channel Island Member at the base[50]. The Channel Island Member is characterized by cyclic siltstone-dolostone couplets with evaporite minerals preferentially being deposited in dolostone layers as nodules and bladed crystals[51]. The Channel Island Member contains massive beds of sandstone near its top and is overlain by the Middlebrun Bay Member[50]. This 0.5-3m thick, stromatolitic dolostone-chert represents the shoreline of the saline lake (Ref. 28 main text). The Middlebrun Bay Member is overlain by the Firehill Member, which consists of massive to finely laminated red siltstones with sporadic intraformational mass-flow conglomerate beds. Deposition occurred on mud- and sand-flats with a near-surface, saline water table[28,51] (Ref. 28 main text). Sulfate minerals throughout the Firehill Member have been observed to occur as nodules, bladed crystals, veins, cements and detrital grains, however this study's sample set only consisted of nodules. The Firehill Member is terminated by the appearance of ripple marks and hummocky cross-bedded sandstones and mudstones of the Kama Hill Formation marking transgression of a large water-mass. Together these observations have shaped the view that the Pass Lake and Rossport Formations of the Sibley Group were deposited in predominantly fluvio-lacustrine and sabkha settings although additional work is needed to constrain the influence of marine waters on the system.

Isotopic Measurements

$\Delta^{17}O$ Measurements: We followed the analytical procedure detailed in Refs. 2 and 43. Drill core samples with abundant gypsum nodules were selected for oxygen isotope analyses (Extended Data Table 1). After a thin layer was milled from the outer surface to avoid potential modern contamination, samples were drilled to collect ≈30 mg of material for pre-treatment. Drilled powders were first dissolved into a 0.1 M sodium hydroxide – 0.05 M diethylenetriaminepentaacetic acid (DTPA) solution to extract sulfate into solution and remove any non-sulfate oxygen-bearing species[52]. The extracted sulfate samples were then reprecipitated at 80˚C by acidifying with double distilled 6 M hydrochloric acid followed by the addition of drops of concentrated barium chloride solution. This dissolution and reprecipitation was repeated

to further eliminate possible contaminations. Approximately 10 mg of purified $BaSO_4$ was then loaded onto a 316L stainless steel plate and placed under a bromine pentafluoride (BrF_5) atmosphere for 12 hours to eliminate any water absorbed to the samples. Molecular oxygen was generated from the samples using a CO_2-laser fluorination system. Although approximately 25 µmol of O_2 gas was generated (25-35% yield) for each sample, this process is not observed to induce any significant isotopic fractionation for $\Delta^{17}O$ values[53]. Molecular O_2 produced during the fluorination process was then taken through a number of cryo-focusing steps to remove condensable gases followed by collection onto mol sieve 5A at -196˚C prior to expansion into the sample bellows of a Thermo MAT 253 mass spectrometer for dual-inlet analysis.

$\Delta^{17}O$ values are expressed arithmetically as follows:

$$\Delta^{17}O = \delta^{17}O - 0.5305 \times \delta^{18}O$$

where 0.5305 represents a high temperature limit for ^{16}O-^{17}O-^{18}O fractionation[54-56], and

$$\delta^{i}O = ([^{i}R_{sample}/^{i}R_{VSMOW}] - 1) \times 1000$$

where $^{i}R = {}^{i}O/^{16}O$, i = 17 or 18, and calculated values are reported as parts per thousand (‰) on the V-SMOW scale. We used an arithmetic definition for $\Delta^{17}O$ instead of a logarithmic definition [eg., $\Delta^{17}O = ln(\delta^{17}O+1) - 0.5305\bullet\bullet\ ln(\delta^{18}O+1)$] to allow for direct comparison between measured $\Delta^{17}O$ values and $\Delta^{17}O$ values calculated from the isotope-mass-balance model. Although a logarithmic definition for $\Delta^{17}O$ is commonly used due to a weaker dependence on the isotopic composition of reference material[57,58], differences between arithmetic and logarithmic $\Delta^{17}O$ values calculated in this study were typically on the order of 0.001‰. This deviation is much less than the uncertainty on $\Delta^{17}O$ analyses (1σ = 0.05‰), estimated based on multiple measurements of the same $BaSO_4$ calibrated against UWG-2 (taken to have $\delta^{18}O$ = +5.80‰ and $\delta^{17}O$ = 3.016‰ on the VSMOW scale; Extended Data Table 1; Extended Data Fig. 1).

$\delta^{18}O$ Measurements: Since the low yield of laser-fluorination techniques leads to a significant fractionation in the measured $\delta^{18}O$ value of sulfates, we combusted sulfate samples and measured the major oxygen isotope composition on the resulting carbon monoxide (CO)[44]. Measurements for $\delta^{18}O$ values were made on the same aliquots of sample used for $\Delta^{17}O$ analysis that underwent the DTPA – reprecipitation treatment. Analyses were performed using a

Temperature Conversion Elemental Analyzer connected to a Conflo-III and a Thermo MAT 253 mass spectrometer in continuous-flow mode. The estimated total analytical error for $\delta^{18}O$ analyses is estimated to be less than 0.5‰ from repeated measurements of laboratory standards (USGS34 $\delta^{18}O$ = -27.80‰; IAEA-NO3 $\delta^{18}O$ = 25.6‰; USGS35 $\delta^{18}O$ = +56.80‰)[43].

$\delta^{34}S$ and $\Delta^{33}S$ Measurements: Sulfur isotope measurements were made purified $BaSO_4$ produced from the DTPA – re-precipitation treatment for oxygen isotope analysis. Approximately 10 mg of barite powder was reacted with 15 mL of Thode reduction solution at 100˚C for at least 2 hours[59]. Powders reacted completely to produce H_2S that was carried through a condenser in a N_2 gas stream and bubbled into a 0.4 M zinc acetate solution where the H_2S was quantitatively captures as ZnS. Samples were then reacted with ~5-10 drops of 0.2 M $AgNO_3$ solution to covert ZnS to Ag_2S. The Ag_2S was then filtered, collected and dried for 12 hours. Approximately 3 mg aliquots of dried Ag_2S were then loaded into nickel bombs and heated to 250˚C for 12 hours under a fluorine gas atmosphere to generate SF_6 gas for analysis. The resulting SF_6 was purified cryogenically and chromatographically before isotopic analysis on a Thermo MAT 253 mass spectrometer in dual-inlet mode.

Sulfur isotope compositions are expressed as follows:

$$\delta^{i}S = ([^{i}R_{sample}/^{i}R_{V\text{-}CDT}] - 1) \times 1000$$

where $^{i}R = {}^{i}S/^{32}S$, i = 33 or 34, and V-CDT indicates the Vienna Canon Diablo Troilite scale. $\Delta^{33}S$ values are expressed as follows:

$$\Delta^{33}S = \delta^{33}S - 1000 \times ([1+ (\delta^{34}S/1000)]^{0.515} - 1)$$

Results were normalized against repeat analyses of international reference material IAEA-S1 which we take to have $\delta^{34}S$ = -0.3‰ and $\Delta^{33}S$ = -0.061‰ on the V-CDT scale. The estimated (1σ) total analytical uncertainty on the entire procedure is estimated to be better than 0.1‰ for $\delta^{34}S$ and 0.01‰ for $\Delta^{33}S$ (Extended Data Table 1).

Model Description

We adapted an analytical solution to a steady-state model[3] for the $\Delta^{17}O$ value of tropospheric O_2 that allows for variation in pO_2, pCO_2, stratosphere-troposphere transport and stratospheric O_2-O_3-CO_2 photochemistry[55,60] (Extended Data Table 2). As described below, we made three primary changes to this model. First, we cast the model solution into a form that incorporated pO_2, pCO_2, and *GPP* estimates relative to a set of reference values for Pre-Anthropogenic Levels (PAL; Extended Data Table 2). Second, we re-arranged the model solution to solve for *GPP* as a function of measured $\Delta^{17}O$ values and model parameters. Third, we inverted the model solution to solve for pO_2 as a function of measured $\Delta^{17}O$ values, other model parameters, and inferred *GPP*. We present the equations used to enact these changes in the supplementary information and describe the constraints we applied to the various model parameters below. Finally, we outline our Monte Carlo approach for estimating probability densities for *GPP* and pO_2.

Constraints on Model Parameters

pCO_2: One-dimensional radiative convective models have been used to estimate pCO_2 levels required to maintain Earth surface temperatures of 273˚K and 288˚K, placing broad upper and lower limits on 1.4 Ga pCO_2 of 1 and 100 PAL respectively (Extended Data Fig. 2)[61]. A further accounting of transport process through extrapolation of results from the CAM3 general circulation model refines these values considerably[62]. For example, to maintain an average surface temperature of 288˚K under a pure CO_2 atmosphere an upper estimate of 1.4 Ga pCO_2 is calculated to be 30 PAL, and an atmosphere including 1 PAL N_2 and 10^{-4} Bar of methane provides a lower bound at 5 PAL pCO_2 (Extended Data Fig. 2)[62]. These ranges are consistent with results from the COPSE Earth System model that put forward a 1.4 Ga pCO_2 range of 8-20 PAL (Extended Data Fig. 2)[63].

Geochemical approaches have also been used in constraining Proterozoic CO_2 levels. A singular previous study attempted to constrain 1.4 Ga pCO_2 by relating carbon isotope fractionations between organic matter in microfossils and surrounding carbonate to extracellular CO_2 levels[64]. Such estimates remain poorly calibrated in the laboratory, especially at high CO_2 levels so we do not include the suggested 10-200 PAL range put forward through this approach. Quantification of silicate weathering in response to different pCO_2 levels in profiles of 1.8 (pCO_2 = 45 PAL) and 1.1 (pCO_2 = 1 PAL) Ga paleosols suggests pCO_2 levels were between ≈2-20 PAL when extrapolated to 1.4 Ga[65]. A lower bound of 2 PAL approximates the CO_2 threshold (350-550 ppm) thought to maintain an ice-sheet free Paleogene Earth (Extended Data Fig. 2)[66]. Distilling results from these different approaches and considering the robustness of the different results, we set a uniform uncertainty envelope around 1.4 Ga CO_2 levels between 2-30 PAL[62,65] (Extended Data Fig. 2).

pO_2: The presence of $\Delta^{17}O$ anomalies requires a threshold amount of atmospheric oxygen to allow for the inception of photochemical reactions involving ozone. Calculations suggest this threshold exists at a pO_2 value of 0.001 PAL (Extended Data Fig. 2)[19,67], well above levels calculated for the removal of mass independent sulfur isotope anomalies[68]. It is for this reason that Archean samples[69] (Extended Data Table 1) do not bear anomalous $\Delta^{17}O$ signatures[20] even though Archean pCO_2 concentrations were likely at much higher levels than the modern environment.

Studies based on mineral stability observed through iron loss within paleosols estimated that mid-Proterozoic O_2 levels were greater than 0.01 PAL[70]. In contrast, recent work that examines the kinetics involved in oxidizing terrestrial Mn or Fe and tracking this through the isotopic composition of chromium (Cr) through the mid-Proterozoic sedimentary record. Cr-isotope based estimates provide a threshold estimate of mid-Proterozoic pO_2 at $<$ 0.01-0.001 PAL, with evidence for pO_2 levels above this only appearing after 1.2 – 0.8 Ga (Extended Data Fig. 2)[71-73]. Paleosol and Cr-isotope based estimates contrast those suggested through trace metal enrichments and biomarkers in 1.4 Ga shales that have been used to argue for pO_2 levels $>$ 0.04 PAL[74,75]. These estimates are consistent with a broad range of values implied by tracking Zn/Fe ratios of carbonates over the latter 3.5 billion years of Earth history that place pO_2 at less than 0.06 PAL over the mid-Proterozoic[76].

Modeling studies have added to this debate suggesting mid-Proterozoic pO_2 must be much less than 0.4 PAL[77] to be consistent with no evidence for persistent fully oxygenated oceans in preserved marine sediments[78,79] or 0.1 PAL to be consistent with the stability of the stable carbon isotope record[80]. Biological modeling constraints have been provided by calculated O_2 requirements for *Grypiania Spiralis* and were suggested to be between 0.01-0.1 PAL pO_2[81], placing a lower limit on pO_2 upon the emergence of these fossils in the geologic record by 1.4 Ga. Estimates utilizing this logic have been brought down considerably in recent years however to ≈ 0.0015 PAL from calculations based on minimum requirements of simple bilaterians and ≈ 0.004 PAL from experimental results on sponges grown in the laboratory (Extended Data Fig. 2)[82,83].

While all of these studies speak to reduced pO_2 in the mid-Proterozoic compared to more recent Earth history (Extended Data Fig. 2), to date, there is no clear consensus. With this in mind, we remain largely agnostic to the techniques used to derive previous estimates and apply a uniform distribution between a lower limit of 0.001 PAL (0.1% PAL) and an upper limit of 0.1 PAL (10% PAL) as our initial estimate for mid-Proterozoic pO_2 (Extended Data Table 2; Extended Data Fig. 3).

f_{O_2}: Two laboratory studies[22,84] have attempted to quantify different pathways of pyrite oxidation and the proportion of atmospheric O_2 that is incorporated into product sulfate (f_{O_2}). In experiments with *A. Ferrooxidans* it was determined that between 8 and 15% of oxygen in product sulfate was from atmospheric oxygen[22]. In abiotic experiments it was determined that 13% of oxygen in product sulfate was from atmospheric oxygen[22]. Both experiments were conducted at low pH values between 2.2-3[22]. In a second study, abiotic experiments were conducted over a much broader pH range (2-11) and O_2 incorporation into sulfate during pyrite oxidation was determined utilizing both major ($\delta^{18}O$) and minor ($\Delta^{17}O$) oxygen isotopes[84]. In these experiments it was determined that between 21-34% of oxygen in sulfate was sourced from atmospheric oxygen[84]. While it remains difficult to determine the exact proportion of oxygen within sulfate that is sourced from H_2O and O_2, these previous studies provide a conservative range of f_{O_2} between 8-34%. When considering the differences in kinetics between abiotic and biotic pyrite oxidation in modern settings, however, this range can be refined. Experiments and natural observations have shown that biologically mediation can dramatically increase pyrite oxidation kinetics and therefore is more likely to dominate natural surface environments both at present and likely in the past[21,84]. Therefore in this study we assume a uniform distribution of possible f_{O_2} values between 8-15% (Extended Data Table 2; Extended Data Fig. 3).

Oxygen isotope fractionation in O_2-O_3-CO_2 photochemical reaction networks: We follow the approach outlined in Ref. 3 and use the results of the photochemical experiments described in Ref. 60 to constrain the parameters: ρ_0, X_l, X_h, ${}^{17}m^{\mathrm{strat}}_{\mathrm{CO2\text{-}O2}}$, ${}^{17}b^{\mathrm{strat}}_{\mathrm{CO2\text{-}O2}}$. Published fits to the experimental results for $\delta^{18}O^{\mathrm{strat}}_{\mathrm{CO2\text{-}O2}}$ as a function of pO_2-pCO_2 ratios constrain ρ_0 to 1.230 ± 0.325, X_l to 64.0 ± 5.5‰, and X_h to 146 ± 2‰ (all uncertainties 1σ; Extended Data Table 2)[60].

We used these values and their uncertainties to define gaussian probability density functions for ρ_0, X_l, and X_h (Extended Data Fig. 3).

We made a linear least-squares fit to the $\delta^{18}O_{CO2-O2}$ and $\delta^{17}O_{CO2-O2}$ measurements in Extended Data Table 1 in Ref. 60 and used this fit to derive a linear relationship between $\Delta^{17}O^{strat}_{CO2-O2}$ and $\delta^{18}O^{strat}_{CO2-O2}$. The coefficients of the resulting relationship are: $^{17}m^{strat}_{CO2-O2} = 0.5167 \pm 0.0336$ and $^{17}b^{strat}_{CO2-O2} = -8.052 \pm 3.673$ (all uncertainties 1σ; Extended Data Table 2). We used these values and their uncertainties to define gaussian probability density functions for $^{17}m^{strat}_{CO2-O2}$ and $^{17}b^{strat}_{CO2-O2}$ (Extended Data Fig. 3). The coefficients derived here differ slightly from those in Ref. 3 due to the fact that we define $\Delta^{17}O$ values with a slope of 0.5305[85,86] rather than 0.52.

γ: We use an estimate of the mass of the modern atmosphere (5.148×10^{18} kg)[87] and a recent determination of the stratosphere-troposphere mass flux (2.194×10^{17} kg yr^{-1})[88] to derive an updated estimate for the stratosphere-troposphere exchange rate in the modern atmosphere (0.0426 yr^{-1}; Extended Data Table 2). It is not well known how stratosphere-troposphere mass transfer will change under atmospheric states different from the modern. Previous work has explored how the Brewer-Dobson circulation may change with elevated CO_2 levels, and suggests that increasing pCO_2 by a factor of two will increase mass flux across the tropopause by ≈20% with further CO_2 increases only slightly affecting stratosphere-troposphere exchange[89]. As we lack a full quantitative exploration of the impact of mid-Proterozoic atmospheric state on γ, we take a statistical approach here and allow γ to vary by about 50% according to a gaussian probability function defined by a 1σ value of 0.01 (Extended Data Table 2; Extended Data Fig. 3).

θ : We use the calculation procedure described above to define a value for the fraction of stratospheric O_2 taking part in the stratospheric O_2-O_3-CO_2 reaction network under pre-anthropogenic levels (pO_2 = 1PAL; pCO_2 = 1PAL; *GPP* = 1PAL). Within this calculation framework, a value of θ of 0.1156 reproduces the $\Delta^{17}O$ of modern tropospheric O_2 (-0.546‰ under the definition of $\Delta^{17}O$ used here)[25]. Although it is unknown how this value will change under different atmospheric states, we assume that θ is fixed by the development of an ozone layer and hold it constant throughout the calculations presented here.

Model Calculations and Sensitivity

We estimated probability densities for mid-Proterozoic *GPP* by repeating the calculation procedure described above 10,000 times, each time drawing a single estimate for each model parameter according to the distributions shown in Extended Data Fig. 3 and a single estimate for the $\Delta^{17}O$ of mid-Proterozoic sulfate randomly from the dataset measured here (Fig. 1; Extended Data Table 1; Extended Data Fig. 7). A realization of the *GPP* probability density from this Monte Carlo resampling and calculation procedure is shown in Fig. 3 and archived in Supplementary Table 1. We also plot individual *GPP* results against various control parameters of the model in Extended Data Fig. 4. Although we permitted potential variability in $\Delta^{17}O$ due to local processes (e.g., changes in sulfide oxidation through variable f_{O_2}) that may have varied stratigraphically (Extended Data Fig. 7) as well as global ones (e.g., changes to stratospheric oxygen dynamics through a variable stratosphere-troposphere exchange rate), these plots show that *GPP* is most sensitive to variations in pO_2, with a near log-linear relationship between assumed pO_2 and calculated *GPP* (Extended Data Fig. 4B). Much weaker dependencies are apparent on $\underline{f_{O_2}}$ and $\Delta^{17}O_{sulfate}$ Though a small percentage of the calculated *GPP* values are greater than 1 PAL, the sensitivity exercise illustrates that these values require a combination of high pO_2, small $\Delta^{17}O_{sulfate}$ and large $\underline{f_{O_2}}$ (Extended Data Fig. 4). This combination of extreme conditions is unlikely to have characterized the mid-Proterozoic Earth, given the probability distributions derived here (Extended Data Fig. 4).

The strong control of pO_2 on the calculated GPP values led us to investigate more restricted ranges of pO_2 between 0.1% and 1% PAL and between 1% and 10% PAL. In both cases the bimodality seen in the full suite of Monte Carlo calculations (Fig. 3) disappears, and both sets of calculations are well approximated by single-peaked gaussian probability density functions (Extended Data Fig. 5). This confirms that pO_2 is the dominant control on the bimodal structure seen in the full suite of Monte Carlo calculations (Fig. 3), and justifies our division of those results into a pair of gaussian probability density functions, one associated with pO_2 between 0.1% and 1% PAL and another associated with pO_2 between 1% and 10% PAL

We fit the estimated *GPP* probability density to combinations of gaussian probability density functions and found that a pair of such functions well approximated the calculated results (Fig. 3). The parameters describing these two gaussian probability density functions can be found in Supplementary Table 1 and indicate that our measurements of the $\Delta^{17}O$ of mid-Proterozoic sulfate are consistent with two mean values of *GPP* (41±3 % PAL and 6±1 % PAL, where the uncertainty reflects 95% confidence intervals on the mean). As described above we inverted our calculation procedure to estimate the specific pO_2 values that are consistent with each of these *GPP* estimates (Extended Data Fig. 5) and found that the high *GPP* state corresponds to pO_2 of ≈2% PAL, while the low *GPP* state corresponds to pO_2 of ≈0.3% PAL (Supplementary Table 1). This direct relationship between *GPP* and pO_2 is present over a wide range of *GPP* values (Extended Data Fig. 4B) and appears to reflect a fundamental characteristic of the mid-Proterozoic Earth.

Data Availability:

The authors declare that all data supporting the findings of this study are available within the paper and its supplementary information files.

Extended Data Captions:

Extended Data Figure 1. Histograms of existing $\Delta^{17}O$ data through Earth history. Phanerozoic sulfates[2] (light grey), syn-Marinoan CAS[29] (dark grey), post-Marinoan barite[2,39-41,43] (blue), and results from the Sibley sulfates (red).

Extended Data Figure 2: Compiled pCO_2 and pO_2 estimates. Panel A, (PAL, left y axis; ppm, right y axis) Grey band outlines results from 1-D modeling[61] based on temperatures of 273˚K (bottom), 288˚K (top) and changing solar luminosity. Red dotted lines represent extrapolated GCM results[62] from Archean estimates. Green shaded region represents the uncertainty envelope of paleosol-based estimates[65] with the green dotted lines interpolating between estimates at 1800 and 1100 Ma together. Pink shaded region represents estimates based on the COPSE Earth system model[63]. Brown bar represents modeling-based estimates required to prevent a global glaciation at 1100 Ma[90]. Dark blue square is microfossil-based estimate setting maximum limits at 1050 Ma[91,92]. Yellow arrows represent the upper (30 PAL) and lower (2 PAL) limits used in this work. In Panel B, Green arrows represent biologically based estimates; blue arrows represent geochemical estimates; and in red are modeling pO_2 estimates. Purple lines represent the removal of S-MIF[93], a proposed bistability field[94], and constraints on the establishment of a modern-like ozone layer[13,67]. Yellow dashed line represents suggested limits for the removal of deep ocean anoxia[76], and grey dashed line represents the appearance of charcoal.

Extended Data Figure 3: Probability distribution functions for the control parameters of the model. See the text for the justification for the form (gaussian or uniform), the spread (standard deviation or range), and the mean of each distribution.

Extended Data Figure 4: Realization of ≈10,000 Monte Carlo calculations of *GPP* (PAL) relative to various control parameters in the isotope mass balance model. A) Unlike model calculations for the Neoproterozoic, there is no clear strong dependence of *GPP* on assumed pCO_2. B) There is a clear log-linear dependence of the *GPP* estimates on pO_2. C) *GPP* responds weakly to f_{O2}, with large fractions of O_2 in sulfate (which imply smaller $\Delta^{17}O_{O2}$ values) leading to higher estimates of *GPP*. D) The response of *GPP* to $\Delta^{17}O_{sulfate}$ is similar to the response to f_{O2}. Smaller $\Delta^{17}O_{sulfate}$ values imply smaller $\Delta^{17}O_{O2}$ values, which, all else being the same, requires greater *GPP*. E) *GPP* estimates seem largely independent of γ.

Extended Data Figure 5: **Realization of ≈20,000 Monte Carlo calculations of *GPP* (PAL) and pO_2.** In Panel A, results are calculated to be consistent with the $\Delta^{17}O$ measurements in Extended Data Table 1 and the probability distribution functions shown in Extended Data Figure 2, with the exception of pO_2. These calculations assume restricted ranges of pO_2 between 0.1% and 1% PAL (orange histogram) and between 1% and 10% PAL (blue histogram). In both cases the bimodality seen in the full suite of Monte Carlo calculations (Fig. 3) disappears, and both sets of calculations are well approximated by single-peaked gaussian probability density functions. This confirms that pO_2 is the dominant control on the bimodal structure seen in the full suite of Monte Carlo calculations (Fig. 3), and justifies our division of those results into a pair of gaussian probability density functions, one associated with pO_2 between 0.1% and 1% PAL and another associated with pO_2 between 1% and 10% PAL. In Panel B, Results are solutions that are consistent with the $\Delta^{17}O_{sulfate}$ dataset (Extended Data Table 1), the probability density functions shown in Extended Data Figure 1 (with the exception of pO_2), and the mean *GPP* estimates of the two inferred gaussian probability distributions for mid-Proterozoic *GPP* (Fig. 3, main text). *GPP* was allowed to vary in a gaussian fashion between the 95% confidence limits on the *GPP* mean values.

Extended Data Figure 6. Geological map of the Lake Nipigon – northern Lake Superior region adapted from Ref. 28 © 2008 Canadian Science Publishing.

Extended Data Figure 7: Oxygen and sulfur isotope compositions ($\Delta^{17}O$, $\delta^{18}O$, $\delta^{34}S$ and $\Delta^{33}S$) for sulfates from drill hole NI-92-7 plotted against stratigraphic height. Uncertainty on all analyses is smaller than the sizes of the data points.

Extended Data Table 1. Isotopic data and comparisons with previously published results. In Panel A, we present data for Sibley samples measured in this study. Associated errors on total laboratory procedures and analysis are presented in the Methods section. In Panel B, we plot results of a linear regression analysis for $\Delta^{17}O$-$\delta^{18}O$ (n = 64), $\delta^{18}O$-$\delta^{34}S$ (n = 46), $\Delta^{17}O$-$\delta^{34}S$ (n = 46) and $\Delta^{33}S$- $\delta^{34}S$ (n = 46) data from this study along with results from previously published syn-Marinoan CAS[29], and post-Marinoan barite[2,39-41,43]. Correlations are significant if a P value is <0.05. In Panel C, we present summary statistics of $\Delta^{17}O$ results on samples from this study compared to post-Marinan barites[2,39-41,43], syn-Marinoan CAS[29], and Phanerozoic evaporites[2].

Samples were binned in 0.1‰ increments. In Panel D, we present new $\Delta^{17}O$ measurements from Archean barites.

Extended Data Table 2. Summary of reference parameters for model calculations.

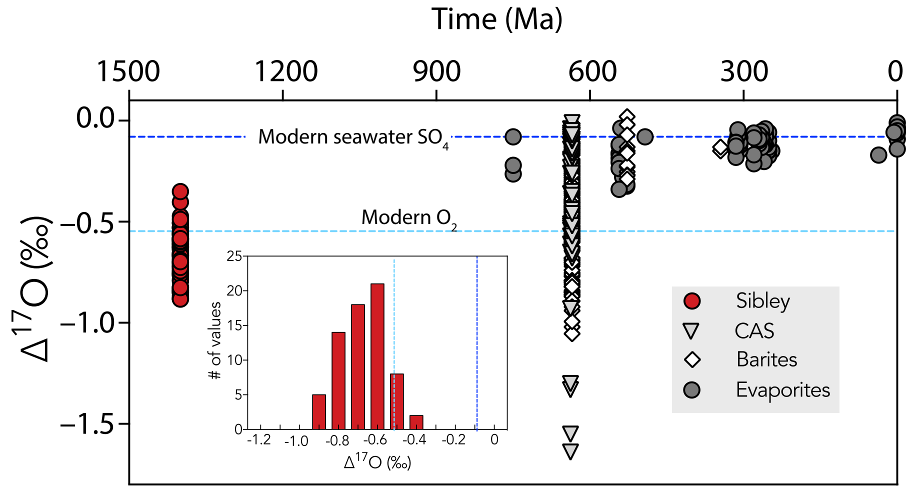

Time (Ma)
1500
1200
900
600
300
0
0.0
−0.5
−1.0
−1.5
$\Delta^{17}O$ (‰)
Modern seawater SO_4
Modern O_2
Sibley
CAS
Barites
Evaporites
# of values
25
20
15
10
5
0
-1.2
-1.0
-0.8
-0.6
-0.4
-0.2
0
$\Delta^{17}O$ (‰)

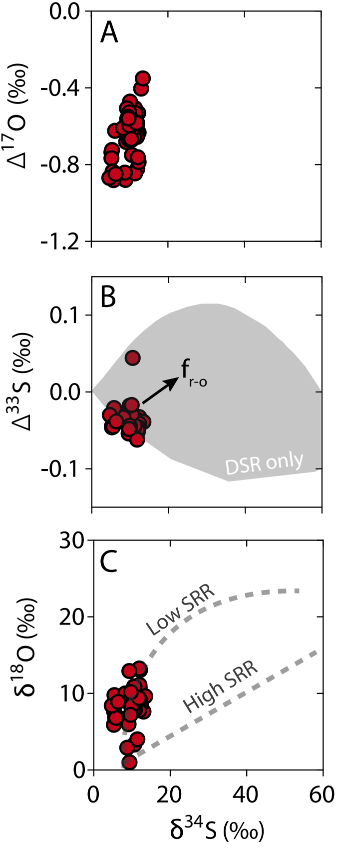
A
0.0
-0.4
-0.8
-1.2
$\Delta^{17}O$ (‰)
B
0.1
0.0
-0.1
$\Delta^{33}S$ (‰)
$f_{r\text{-}o}$
DSR only
C
30
20
10
0
$\delta^{18}O$ (‰)
Low SRR
High SRR
0
20
40
60
$\delta^{34}S$ (‰)

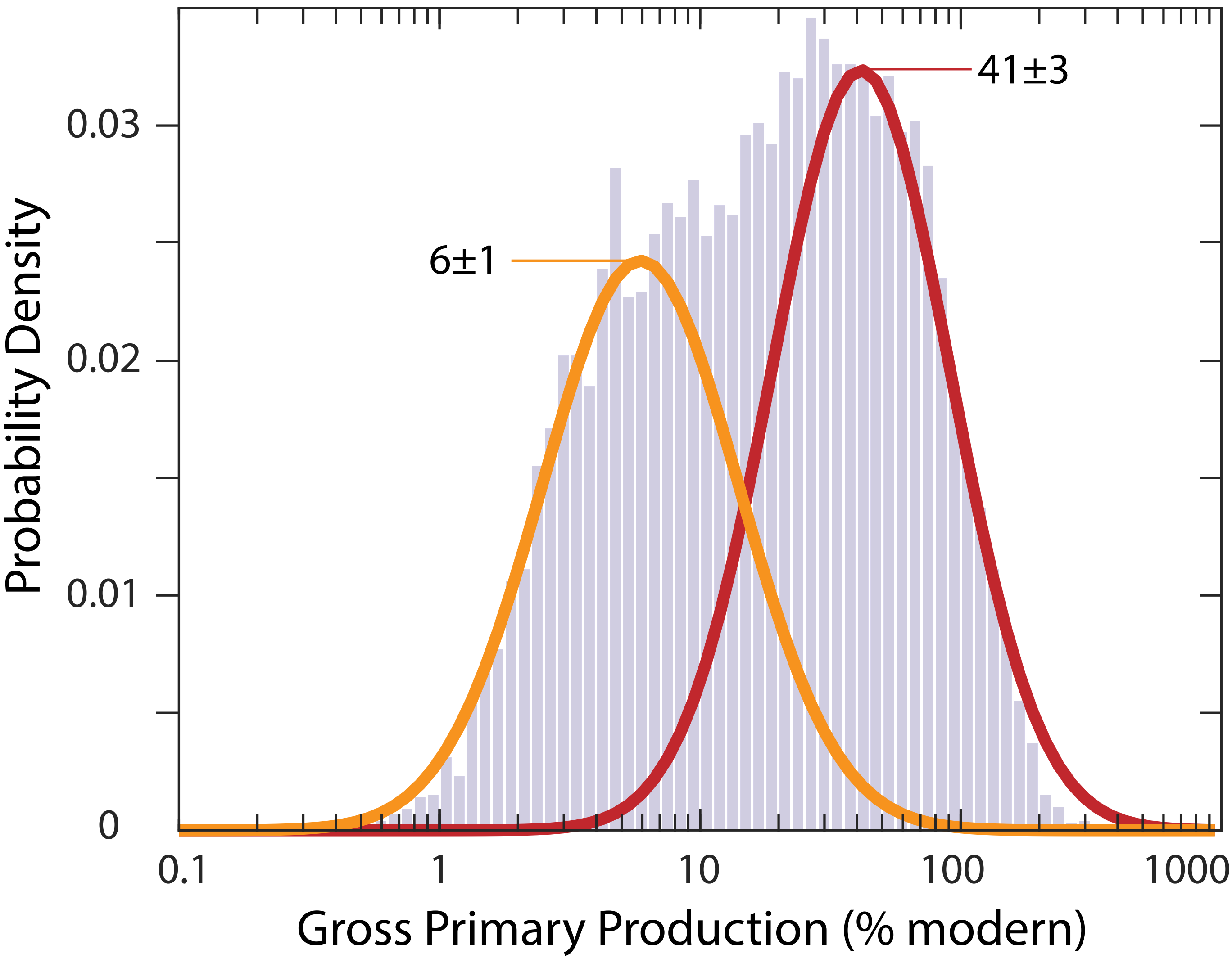
41±3
6±1
0.03
0.02
0.01
0
Probability Density
0.1
1
10
100
1000
Gross Primary Production (% modern)